21st Australasian Fluid Mechanics Conference
Adelaide, Australia
10-13 December 2018

Effects of Wavy Roughness Elements on the Aerodynamic Performance of NACA0012 Airfoil

Wei Gao[1] **and Ravi Samtaney**[1]

[1]Mechanical Engineering, Division of Physical Science and Engineering
King Abdullah University of Science and Technology (KAUST), Thuwal 23955-6900, KSA

Abstract

The effects of 2D surface roughness on the aerodynamic performance of the NACA0012 airfoil ($Re = 5 \times 10^4$, $AoA = 10^\circ$) are investigated with direct numerical simulations (DNS). The DNS are performed with an energy-conservative fourth-order parallel code solving the incompressible Navier-Stokes equations in generalized curvilinear coordinates. Located near the leading edge, the surface roughness elements are characterized with streamwise sinusoidal-wave geometry that is uniform in the spanwise direction but with varying wave number (from $k = 0$ to 12, with $k = 0$ corresponding to the smooth case, chosen as the baseline). The flow structures and and boundary layer separation are quantified, and it is shown that the lift and drag coefficients are strongly affected by separation bubbles that arise. The numerical results reveal that the drag coefficients increase to a peak value and then decrease with increase in wave number, while the lift coefficients decreases strongly for $k \leq 6$ and then become stable. The boundary layer separation is affected by the wavenumber and with an increase in the number of separation bubbles that render the flow more complex. For $k \geq 8$, massive separation occurs and almost covering the suction side of the airfoil dominating the airfoil aerodynamic performance.

Introduction

Flow over rough walls occurs in a wide range of engineering applications, such as piping systems, marine vehicles and urban atmospheric boundary layers [1]. When an aircraft enters a region containing supercooled water droplets, ice accretions of various shapes can form at different locations on its aerodynamic surfaces under different meteorological and flight conditions. In general, two classes of ice accretion, known as rime and glaze, would occur close to the leading edge [2]. The ice accretion effect on aerodynamics has been experimentally and numerically studied for many years [3]. In practice, the ice shape is always complex making it somewhat difficult to generate high-quality mesh for numerical research. Kurz & Kloker (2016) [4] modeled the roughness elements with a finite-size cylinder, and examined the dominant instability mechanism at low *Re*. Serson *et al.* (2017) [5] investigated the effect of spanwise waviness elements on the leading edge with direct numerical simulations (DNS), and found that the wavy roughness elements may decrease or increase the lift coefficient, depending on *Re* and flow regime (pre-stall or post-stall). Thomas *et al.* [6] investigated the development of Tollmien-Schlichting (TS) wave instabilities with the effect of sinusoidal surface waviness elements. Most researches examine spanwise-varying roughness elements whereas effects of streamwise waviness elements are seldom examined. The surface topography has a large effect on the skin friction and near-wall field, as shown by Cheng *et al.* (2018) [7] in the large-eddy simulations of flow over grooved cylinders. This would modify the separation and reattachment locations drastically and thus affect the aerodynamic performance of the airfoil, as previously shown by Goodhand *et al.* (2018) [8], who investigated the the impact of geometric variation near the leading edge.

The main goal of our current research is to investigate the effect of surface roughness elements on the aerodynamic performance of the NACA0012 airfoil. In the present paper, the surface roughness is located close to the leading edge, characterized with sinusoidal wavy elements in the streamwise direction. We present DNS results for the NACA0012 with different wavy roughness elements, $Re = 5 \times 10^4$ ($Re = U_0 C/\nu$, where C is the chord length, U_0 is the free-stream velocity and ν is the kinematic viscosity), at an angle of attack $AoA = 10^\circ$. The paper is organized as follows: we first present the governing equations, numerical method and simulation setup details. Finally, numerical results for the airfoil flows are analyzed and discussed.

Numerical Method

The incompressible Navier-Stokes equations in the generalized curvilinear coordinates are

$$\frac{\partial U^m}{\partial \xi^m} = 0, \quad \frac{\partial \left(\sqrt{g} v_i\right)}{\partial t} + \frac{\partial F_i^m}{\partial \xi^m} = 0, \tag{1}$$

where $\xi^m (m = 1,2,3)$ denotes generalized curvilinear coordinates; and U^m and F_i^m are given by

$$\begin{aligned} U^m &= \sqrt{g} v_j \frac{\partial \xi^m}{\partial x_j} = \sqrt{g} u^m, \\ F_i^m &= U^m v_i + \sqrt{g} p \frac{\partial \xi^m}{\partial x_i} - \frac{1}{Re} G^{mn} \frac{\partial v_i}{\partial \xi^n}, \\ \sqrt{g} &= J^{-1} = \det\left[\frac{\partial x_i}{\partial \xi^j}\right], \; G^{mn} = \sqrt{g} \frac{\partial \xi^m}{\partial x_r} \frac{\partial \xi^n}{\partial x_r}, \end{aligned} \tag{2}$$

where $x_j (j = 1,2,3)$ denotes Cartesian coordinates (note that the spanwise direction $x_3 \equiv z$ is aligned with ξ^3). p is the pressure, v_j is the velocity in the Cartesian system, u^m is the contravariant velocity in the generalized curvilinear coordinates, U^m is the volume flux normal to the surface of constant ξ^m, G^{mn} is the mesh skewness tensor.

The governing equations are discretized as

$$\begin{aligned} \frac{\delta U^m}{\delta \xi^m} &= 0, \\ \sqrt{g} \frac{v_i^{n+1} - v_i^n}{\Delta t} &= \frac{3}{2} C_i^n - \frac{1}{2} C_i^{n-1} + R_i(p^{n+1}) + D_i(v^{n+1}), \end{aligned} \tag{3}$$

where $\delta/\delta\xi^m$ represents the energy conservative fourth-order finite difference operator [9], C_i represent the convective term, D_i and R_i are discrete operators for the viscous term and the pressure gradient term, respectively. These quantities are

$$\begin{aligned} C_i &= -\frac{\delta}{\delta \xi^m}(U^m v_i), \\ R_i &= -\frac{\delta}{\delta \xi^m}\left(\sqrt{g} \frac{\delta \xi^m}{\delta x_i}\right), \; D_i = \frac{\delta}{\delta \xi^m}\left(\frac{1}{Re} G^{mn} \frac{\delta}{\delta \xi^n}\right). \end{aligned} \tag{4}$$

The fractional step method [10, 11] is used to solve the governing equations. The convective term is treated in the skew-

symmetric form to minimize the aliasing error. This method follows the predictor-corrector procedure, and the pressure Poisson equation is solved using the multigrid method with line-relaxed Gauss-Seidel as a smoother. The DNS code have been parallelized using standard MPI-protocol. To achieve optimal load balancing, the mesh is divided into blocks of equal size and each of them is assigned to a unique processor. All the simulations are performed on the Shaheen-Cray XC40 at KAUST.

Simulation Details

The artificial roughness elements are placed near the leading edge on the suction side as shown in Figure 1. These roughness elements are characterized with the sinusoidal-wave structure as follows,

$$y_r = y_0 + h\sin[2\pi(s_0 - 0.05)/\lambda], \tag{5}$$

where y_0 and y_r are smooth and rough wall coordinates, h and λ are the amplitude and wavelength of the roughness elements, respectively. The roughened region starts from $x/C = 0.037$ to $x/C = 0.136$ occupying ten percent of the upper surface length (L_u). In the present work, the roughness height or amplitude is specified at $h = 10^{-3}C$, and the number of the wavy roughness elements (wavenumber) is $k = 0.1L_u/\lambda$. Six cases ($k = 0, 4, 6, 8, 10, 12$) are performed to investigated the effects of different roughness geometries, in which $k = 0$ corresponds to the smooth case.

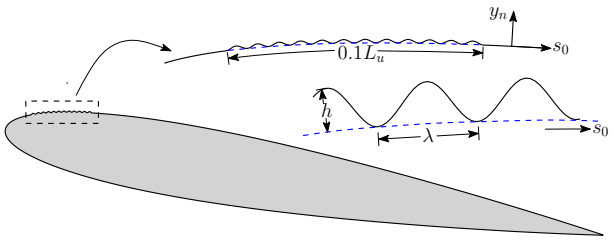

Figure 1: Sketch of the NACA0012 airfoil with artificial wavy roughness elements. s_0 and y_n denotes the local coordinate direction parallel and normal to the smooth airfoil surface ($k = 0$), respectively.

The physical set-up and domain size are illustrated in Figure 2. It should be noted that a sufficiently long spanwise domain size (L_z) is important for the proper development 3D turbulent structures, and here we use $L_z = 0.8C$, as recommended by Zhang & Samtaney (2016) [12] in their direct numerical simulations of flow past an airfoil at $Re = 5 \times 10^4$. For boundary conditions, we impose a uniform flow $(u, v, w) = (1, 0, 0)$ at the inlet, convective boundary condition on the outflow plane and periodic boundary condition in the spanwise direction.

All the simulations are performed with mesh $N_\xi \times N_\eta \times N_z = 2048 \times 256 \times 256$, and the time step is restricted by the advective speed CFL condition (CFL $= 0.8$). The maximum wall units η^+ is around 0.9 (based on local streamwise u_τ and mesh size) to ensure that the near-wall region is fully resolved. The maximum wall units in ξ- and z-directions are less than 10 in the turbulent region. The total simulation time is about $60C/U_0$, and only the last $45C/U_0$ time units are utilized for analysis.

Numerical Results

The time- and spanwise-averaged pressure coefficient (C_p) and skin friction coefficient (C_f) are plotted in Figures 3 and 4, respectively. We observe that C_p strongly decreases (also refers to decreasing the adverse pressure gradient) with increasing roughness wavenumber k ($k \leq 8$) around the roughened region,

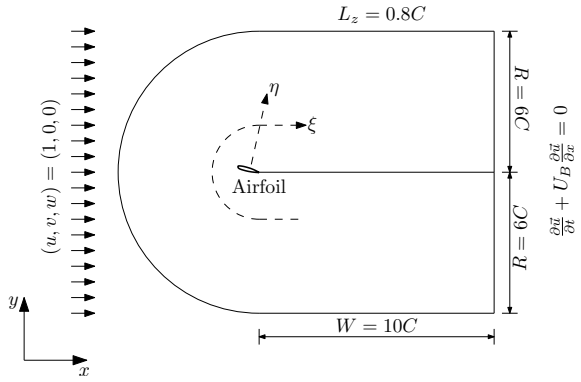

Figure 2: Sketch of the computational domain.

and then increasing gently from $k = 8$ to $k = 12$. The sudden change at $k = 8$ indicates that this may be a critical case, and is discussed later. Not surprisingly, these differences are not obvious on the pressure side. The C_f in Figure 4 indicates separation and reattachment, with a small separation bubble formation near the leading edge for the smooth case, as shown in Figure 5(a) and 6(a). With the increasing of the roughness wave number, more separation bubbles are generated not only in the roughened region but also in the smooth region. The flow structure in the roughened region is even more complex with "oscillating" C_f as shown in Figure 4.

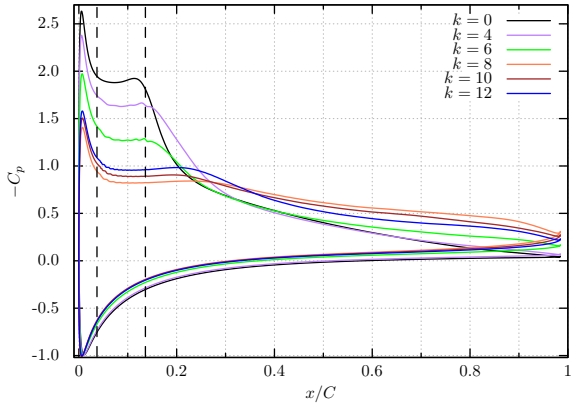

Figure 3: Distribution of the time- and spanwise-averaged pressure coefficient C_p around the airfoil. The black dash lines denotes the boundary of the roughened region.

For the baseline case ($k = 0$), a small separation bubble ($0.022 \leq x/C \leq 0.194$) is observed near the leading edge, which fully covers the roughed region ($0.037 \leq x/C \leq 0.136$). For $k = 4$, the main separation bubble is stretched, and a secondary separation bubble forms on the windward side of the first roughness element. For $k = 6$, two secondary separation bubbles form in the roughened region, as shown in Figure 6, and one separation bubble is noted near the trailing edge. Similar to $k = 4$, these secondary bubbles are formed on the windward side of the roughness elements. As mentioned above, $k = 8$ appears to be a critical value for the wavenumber, beyond which massive separation occurs on the suction side as shown in Figure 5. When the roughness wavenumber increases ($k \geq 8$), the main separation bubble is compressed, eventually bifurcating into two bubbles for $k = 12$. For $k < 8$ the massive separation is strong but smaller in size and covers only 20% of the chord length. However for $k \geq 8$ the massive separation is weak (consider the C_f

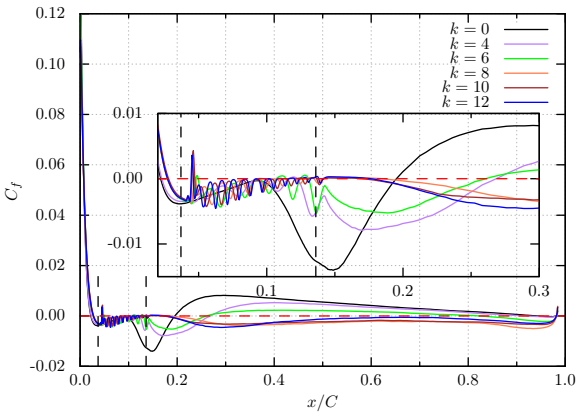

Figure 4: Distribution of the time- and spanwise-averaged friction coefficient C_f on the suction side.The black dash lines denotes the boundary of the roughened region, and the red dashed lines denotes $C_f = 0$.

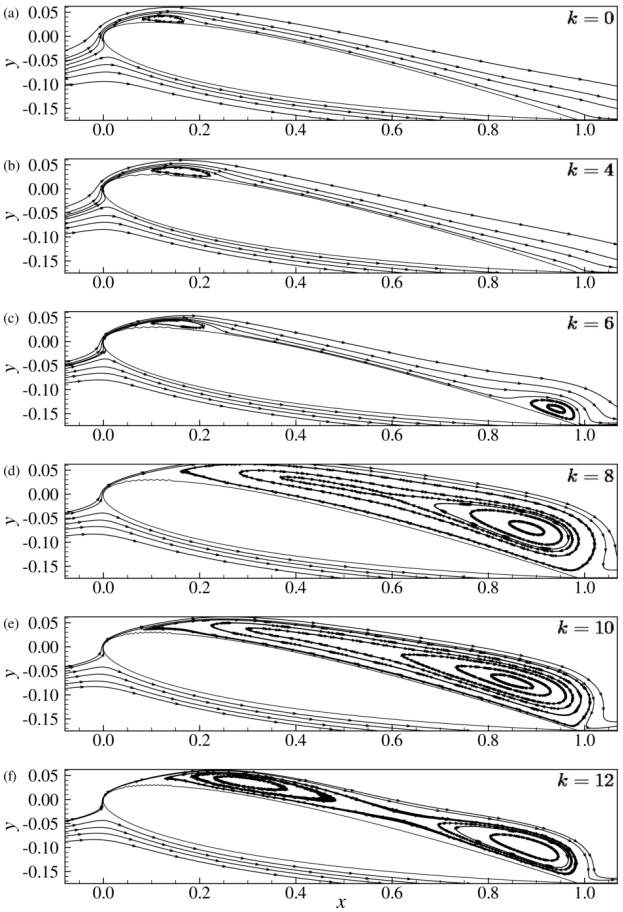

Figure 5: Streamlines of the time and spanwise-averaged flow field for different roughness wave number.

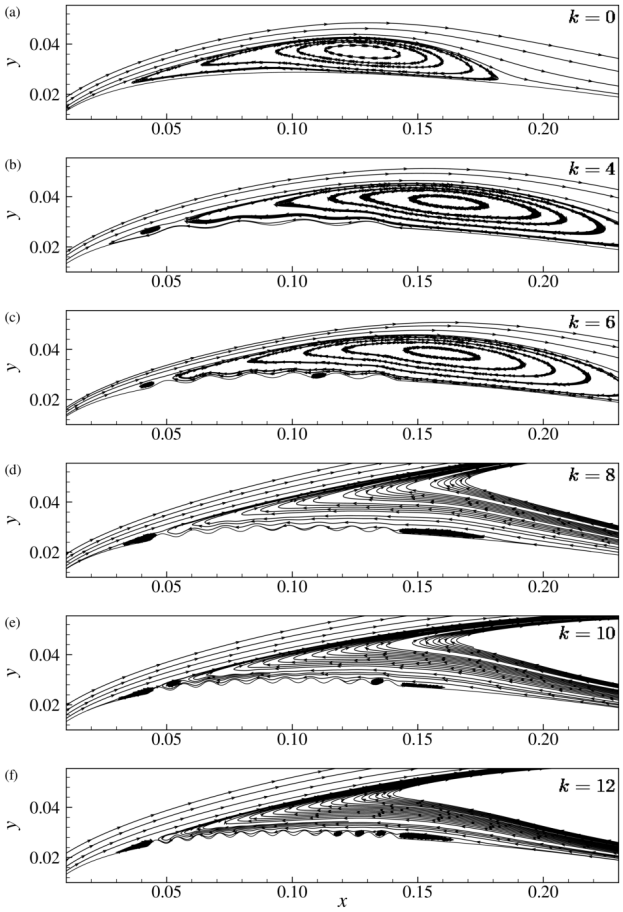

Figure 6: Streamlines of the time and spanwise-averaged flow field near the roughed region for different roughness wave number.

magnitude in Figure 4) but larger in size, covering about 80% of the chord length. Meanwhile, a secondary separation bubble is formed at the leeward side of the last roughness element for $k \geq 8$ as shown in Figure 6.

These separation and reattachment imply strong effects on the aerodynamic performance (lift and drag coefficients) of these airfoils. The variation of the lift coefficient C_L vs. k is plotted in Figure 7. It is observed that C_L strongly decreases for $k \leq 6$, with much smaller variations for $6 \leq k \leq 12$ and the maximum C_L occurring at the critical wavenumber $k = 8$ within this range. The variation of the drag coefficient C_D vs. k is plotted in Figure 8. The peak value of C_D occurs in the critical case $k = 8$, with strong increase for $k \leq 6$. For $k \geq 8$, the variation of C_D is not so intense, very similar to the behavior of C_L. One possible reason is that $k = 8$ is a critical case, after which massive separations occur, and the aerodynamic performance is dominated by these large separation bubbles.

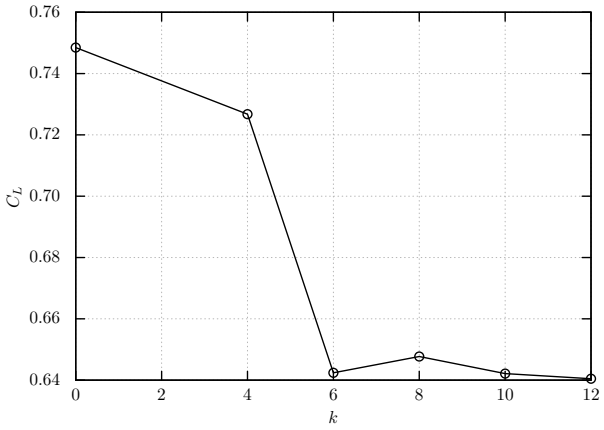

Figure 7: Variation of the lift coefficient C_L with the roughness wave number k.

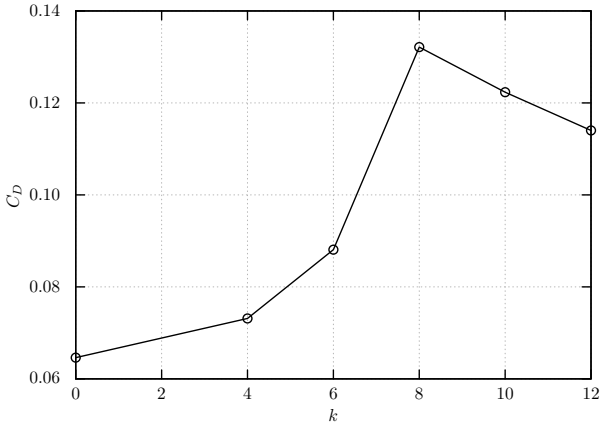

Figure 8: Variation of the drag coefficient C_D with the roughness wave number k.

Conclusions

The effect of streamwise sinusoidal-wavy roughness elements on the aerodynamic performance of the NACA0012 airfoil is systematically investigated with direct numerical simulations (DNS) at $Re = 5 \times 10^4$, $AoA = 10^\circ$. For $0 \leq k \leq 6$, the main separation bubble is stretching around the roughened region, and secondary separation bubble occurs at the windward side of the roughness elements. For $8 \leq k \leq 12$, the main separation bubble is compressed and finally breaking into two bubbles for $k = 12$. Meanwhile, a secondary separation bubble is formed at the leeward side of the last roughness element. The case of $k = 8$ is a critical case, after which massive separation occurs on the upper surface, and drastically affects the drag coefficient. Our future plan is to focus on the effect of the pressure gradients in different cases, and comparisons of high-order turbulence statistics.

Acknowledgements

The work was supported by the KAUST office of Competitive Research Funds under Award No. URF/1/1394-01 and baseline research funds of R. Samtaney. The Shaheen-Cray XC40 at KAUST was utilized for all the simulations.

References

[1] Jiménez, J., Turbulent flows over rough walls, *Annu. Rev. Fluid Mech.*, **36**, 2004, 173–196.

[2] Cebeci, T., Calculation of flow over iced airfoils, *AIAA J.*, **27**, 1989, 853–861.

[3] Bragg, M., Aircraft aerodynamic effects due to large droplet ice accretions, *AIAA*, **826**, 1996, 1–16.

[4] Kurz H. B. E. and Kloker M. J., Mechanisms of flow tripping by discrete roughness elements in a swept-wing boundary layer, *J. Fluid Mech.*, **796**, 2017, 158–194.

[5] Serson D., Sherwin S. J. and Meneghini J. R., Direct numerical simulations of the flow around wings with spanwise waviness, *J. Fluid Mech.*, **826**, 2017, 714–731.

[6] Thomas, C., and Mughal S. and Ashworth R., Development of Tollmien-Schlichting disturbances in the presence of laminar separation bubbles on an unswept infinite wavy wing, *Phys. Rev. Fluids*, **2**, 2017, 043903.

[7] Cheng W., Pullin D. I. and Samtaney R., Large-eddy simulation of flow over a grooved cylinder up to transcritical Reynolds numbers, *J. Fluid Mech.*, **835**, 2018, 327–362.

[8] Goodhand, M. N., and Miller, R. J. and Lung, H. W, The impact of geometric variation on compressor two-dimensional incidence range, *J. Turbomach*, **137**, 2015, 021007.

[9] Morinishi Y., Lund T. S., Vasilyev O. V. and Moin P., Fully conservative higher order finite difference schemes for incompressible flow, *J. Comput. Phys.*, **143**, 1998, 90–124.

[10] Zang Y., Street R. L. and Koseff J. R., A non-staggered grid, fractional step method for time-dependent incompressible Navier-Stokes equations in curvilinear coordinates, *J. Comput. Phys.*, **114**, 1994, 18–33.

[11] Zhang W., Cheng W., Gao W., Qamar A. and Samtaney R., Geometrical effects on the airfoil flow separation and transition, *Comput. Fluids*, **116**, 2015, 60–73.

[12] Zhang W. and Samtaney R., Assessment of spanwise domain size effect on the transitional flow past an airfoil, *Comput. Fluids*, **124**, 2016, 39–53.